Influence of Rotor Iron Bridge Position on DC-winding-induced Voltage in Wound Field Switched Flux Machine Having Partitioned Stators

Zhongze Wu[1*], *Z. Q. Zhu*[2], *Chao Wang*[2], *Wei Hua*[1], *Kai Wang*[3] *and Wentao Zhang*[1]

(1. School of Electrical Engineering, Southeast University, Nanjing 210096, China;

2. Department of Electronic and Electrical Engineering, University of Sheffield, Sheffield S10 2TN, UK;

3. College of Automation, Nanjing University of Aeronautics and Astronautics, Nanjing 211106, China)

Abstract: In this study, the influence of the position of the rotor iron bridge on the DC-winding-induced voltage pulsation in a partitioned stator wound field switched flux machine is investigated. Analytical and finite element (FE) analyses show that both the open-circuit and on-load DC-winding-induced voltages can be minimized by positioning the rotor iron bridge adjacent to the inner air gap closer to the DC winding. This is due to a smoother inner air-gap magnetic reluctance while maintaining the average electromagnetic torque at 92.59% of the maximum value. The analyzed machine with the rotor iron bridge adjacent to the inner air gap is prototyped, and the experimental results validate the analytical and FE results.

Keywords: DC winding induced voltage, flux switching, iron bridge, partitioned stator, switched flux, wound field

1 Introduction

Nowadays the unstable supply chain and price of rare earth element materials may limit the large-scale application of permanent magnet (PM) machines in electric vehicles and many other applications [1-4]. Alternatively, wound field synchronous machines in which the field excitation is provided by a DC winding can be applied to address this challenge [5], which can be divided into two categories according to the location of the DC winding.

One is a wound rotor synchronous machine with rotor accommodation for DC winding [6], and the other is a wound-stator synchronous machine in which both the DC and AC windings are placed in the stator. The rotor of the wound-stator synchronous machines is simple and robust and has neither magnets nor coils, similar to switched reluctance machines [7]. Single-and three-phase wound-stator synchronous machines with a single stator were analyzed in Refs. [8-13], respectively. In Ref. [14], a new type of wound-stator synchronous machine with two stators wound by DC winding and AC windings separately is proposed and analyzed; for example, the 12/10-stator-pole partitioned stator (PS) wound field switched flux (WFSF) (PS-WFSF) machine, as shown in Fig. 1. Owing to higher space utilization, PS-WFSF machines can exhibit a higher torque density than conventional WFSF machines with a single stator [14].

In Refs. [13, 15], the DC windings in WFSF and PS-WFSF machines suffer from induced voltage pulsation, which causes DC current pulsation in DC winding, challenges the DC power supply, and deteriorates the control performance. In Ref. [13], the experimental results show that the DC-winding-induced voltage causes a 19% DC winding current ripple when the prototype is rotating at 500 r/min. In

Manuscript received March 12, 2021; revised April 6, 2021; accepted May 31, 2021. Date of publication September 30, 2021; date of current version August 3, 2021.

* Corresponding Author, E-mail: zzwu@seu.edu.cn

Digital Object Identifier: 10.23919/CJEE.2021.000022

Ref. [15], skewing is introduced to reduce the open-circuit DC-winding-induced voltage, based on the deduced harmonic orders.

In this study, the influence of the position of the rotor iron bridge on the DC-winding-induced voltage in the PS-WFSF machine is investigated, based on the contents reported in Ref. [16]. In Section 2, the machine topology and operation principle of the PS-WFSF machine are introduced. In Section 3, DC-winding-induced voltage harmonics are analytically modeled, and it shows that the DC-winding-induced voltage harmonic contents can be effectively suppressed by designing an appropriate position of the rotor iron bridge, which is verified by finite element (FE) analysis in Section 4. The prototype is built and tested in Section 5 to validate the analytical and FE results, followed by the conclusions in Section 6.

2 PS-WFSF machine

As shown in Fig. 1, the stator in the analyzed 12/10-stator/rotor-pole PS-WFSF machine consists of an outer stator wound by AC windings and an inner stator wound by DC winding. Different from the double stator machines in which two stators are electromagnetically duplicated [17-23], in PS-WFSF machines they produce armature and excitation magnetic fields in the air-gaps, respectively.

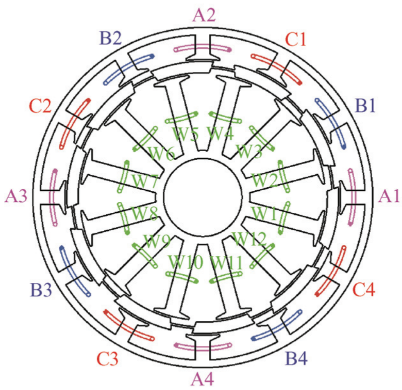

Fig. 1 Cross-section of the 12/10-pole PS-WFSF machine having rotor iron bridge

Fig. 2a shows a single lamination block of a PS-WFSF machine, which has a sandwiched cup rotor consisting of several rotor iron pieces connected by the rotor iron bridge as shown in Fig. 2b, similar to the magnetic gear analyzed in Ref. [24]. The rotor iron bridge can help to ease the assembling difficulty by connecting the rotor iron pieces.

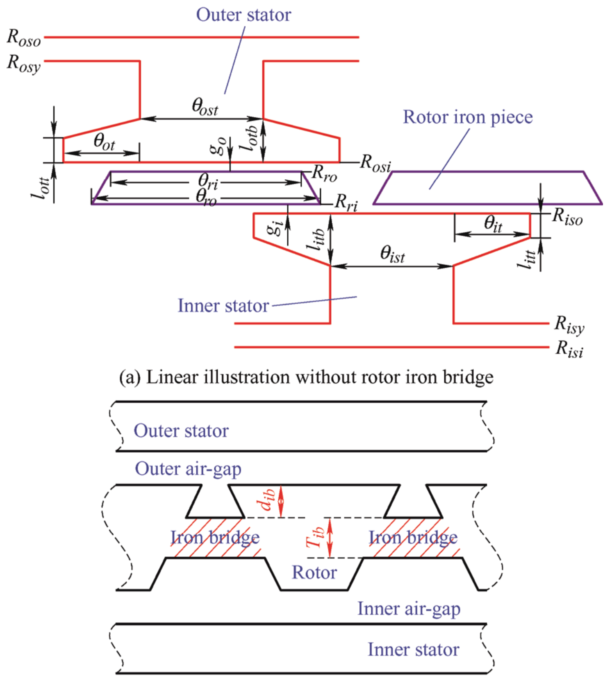

(b) Linear illustration of rotor iron bridge

Fig. 2 Linear illustration of 12/10-pole PS-WFSF machine

The dimensional parameters of the analyzed 12/10-pole PS-WFSF machine are listed in Tab. 1, which can be referred to in Fig. 2. Based on the restrictions of the dimensions from L_{axial} to L_{itb} shown in Tab. 1, other dimensions in the same table are obtained by global optimization with a genetic algorithm for the maximum average electromagnetic torque when the machine operates in brushless AC (BLAC) mode with zero d-axis current control, i_d=0. It should be noted that the position and thickness of the rotor iron bridge, that is, d_{ib} and T_{ib}, are not considered in the global optimization. In this study, the thickness is fixed at T_{ib}=0.5 mm to reduce the torque density, while the influence of its position d_{ib} on the DC-winding-induced voltage is investigated.

The key electromagnetic performances of the original 12/10-pole PS-WFSF machine without iron bridge are listed in Tab. 2.

Tab. 1 Key dimensions of the 12/10-pole PS-WFSF machine

Item	PS-WFSF
Stack length, L_{axial}/mm	50
Outer radius of outer stator, R_{oso}/mm	45
Inner radius of inner stator, R_{isi}/mm	10.4
Width of outer air-gap, g_o/mm	0.5
Width of inner air-gap, g_i/mm	0.5
Length of outer stator tip top, l_{ott}/mm	0.5
Length of outer stator tip bottom, l_{otb}/mm	1.5
Length of inner stator tip top, l_{itt}/mm	0.5
Length of inner stator tip bottom, l_{itb}/mm	1.5
Yoke radius of outer stator, R_{osy}/mm	43
Inner radius of outer stator, R_{osi}/mm	36.5
Radius of rotor inner surface, R_{ri}/mm	33
Yoke radius of inner stator, R_{isy}/mm	12.5
Arc of outer stator tooth, θ_{ost}/(°)	6
Arc of outer stator tip, θ_{ot}/(°)	4
Arc of rotor piece outer edge, θ_{ro}/(°)	27
Arc of rotor piece inner edge, θ_{ri}/(°)	24
Arc of inner stator tooth, θ_{ist}/(°)	7
Arc of inner stator tip, θ_{it}/(°)	5

Tab. 2 Key performance of the original 12/10-pole PS-WFSF machine without iron bridge

Item	PS-WFSF
Rated rotor mechanical speed, Ω_r/(r/min)	400
DC winding stack copper loss, p_{cuf}/W	60
Number of turns per DC coil, N_{fc}	90
DC winding current, I_f/A	3.64
AC windings stack copper loss, p_{cua}/W	60
Number of turns per AC coil, N_{ac}	18
AC windings phase current, I_{rms}/Arms	15.24
Rated AC windings phase back-EMF @400 r/min, E_{rmsr}/Vrms	4.08
Rated on-load average electromagnetic torque, T_a/(N • m)	2.93
Rated on-load average electromagnetic power @400 r/min, P_{ar}/W	122.53

Similar to other types of stator-excitation machines, the operation principle of PS-WFSF machines can be explained by the magnetic gearing effect [12, 25-27]. Due to the modulation effect of the rotor on the DC winding MMF and AC windings MMF, pairs of synchronized open-circuit and armature reaction air-gap field harmonics will be generated, and hence the average electromagnetic torque will be produced in the air gap.

3 DC-winding-induced voltage

3.1 Inner air-gap permeance

Based on Refs. [27-28], the inner air-gap permeance $\Lambda_i(\delta, t)$ can be expressed as

$$\Lambda_i(\delta,t) \approx \frac{g_i}{\mu_0}\Lambda_{is}(\delta)\Lambda_{ir}(\delta,t) \quad (1)$$

where g_i is the inner air-gap width, μ_0 is the vacuum permeability, δ is the spatial mechanical position of the inner air gap, and $\Lambda_{is}(\delta)$ is the inner air-gap permeance with the slotted inner stator and slotless rotor inner side, as shown in Fig. 3a. $\Lambda_{ir}(\delta, t)$ is the inner air-gap permeance function with a slotless inner stator and slotted rotor inner side, as shown in Fig. 3b. They can be expressed as Fourier series as

$$\Lambda_{is}(\delta) = \Lambda_{is0} + S_{is}\sum_{i=1}^{\infty} M_{isi}\cos(iN_s\delta) \quad (2a)$$

and

$$\Lambda_{ir}(\delta,t) = \Lambda_{ir0} + S_{ir}\sum_{j=1}^{\infty} M_{irj}\cos\left[jN_r\left(\delta-\Omega_r t-\theta_0\right)\right] \quad (2b)$$

where $S_{is}=2\Lambda_1/\pi$, $S_{ir}=2\Lambda_2/\pi$, $M_{isi}= -\sin(iN_s\theta_1)/i$, $M_{irj}=\sin(jN_r\theta_2)/j$. Λ_{is0} and Λ_{ir0} are the DC components of Λ_{is} and Λ_{ir}, respectively. N_s and N_r are the number of stator and rotor poles, respectively. θ_1 is half the sum of the inner stator tooth arc and inner stator tooth tip arc. θ_2 is half the inner arc of the rotor iron piece. Ω_r is the mechanical speed of the rotor. θ_0 is the initial rotor position.

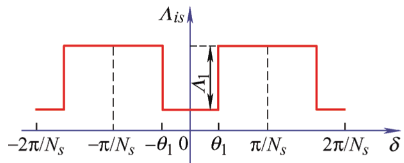

(a) $\Lambda_{is}(\delta)$

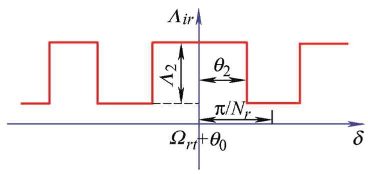

(b) $\Lambda_{ir}(\delta, t)$

Fig. 3 Illustration of inner air-gap permeance components $\Lambda_{is}(\delta)$ and $\Lambda_{ir}(\delta, t)$

Based on Eqs. (2a) and (2b), $\Lambda_{is}(\delta)\Lambda_{ir}(\delta, t)$ in Eq. (1) can be rewritten as

$$\Lambda_{is}(\delta)\Lambda_{ir}(\delta,t) = \Lambda_{is0}\Lambda_{ir0} + \Lambda_{ir0}S_{is}\sum_{i=1}^{\infty}M_{isi}\cos a + \Lambda_{is0}S_{ir}\sum_{j=1}^{\infty}M_{irj}\cos b + \frac{1}{2}S_{is}S_{ir}\sum_{i=1}^{\infty}\sum_{i=1}^{\infty}M_{isi}M_{irj}(\cos c+\cos d) \quad (3)$$

where a, b, c, and d can be given by

$$\begin{cases} a = iN_s\delta \\ b = jN_r\delta - jN_r\left(\Omega_r t + \theta_0\right) \\ c = \left(iN_s + jN_r\right)\delta - jN_r\left(\Omega_r t + \theta_0\right) \\ d = \left(iN_s - jN_r\right)\delta + jN_r\left(\Omega_r t + \theta_0\right) \end{cases} \tag{4}$$

3.2 DC winding MMF and AC windings MMF

As shown in Fig. 4, the air-gap DC winding MMF F_f is a square wave with the air-gap circumferential position δ, which can be expressed as Fourier series

$$\begin{cases} F_f\left(\delta\right) = S_f \sum_{m=1}^{\infty} M_{fm} \sin p \\ p = \frac{1}{2}\left(2m-1\right)N_s\delta \end{cases} \tag{5}$$

where S_f=$4N_{fc}I_f/\pi$, M_{fi}=$\cos[(2m-1)N_s\theta_1/2]/(2m-1)$.

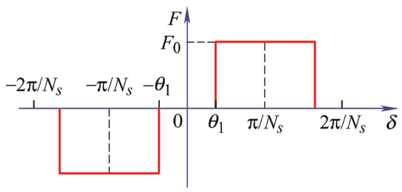

Fig. 4 Illustration of DC winding MMF F_f

The AC windings are injected by three-phase symmetrical sinusoidal currents, which can be expressed as

$$\begin{cases} i_A = \sqrt{2}I_{RMS}\sin\left(\omega_e t\right) \\ i_B = \sqrt{2}I_{RMS}\sin\left(\omega_e t - \frac{2\pi}{3}\right) \\ i_C = \sqrt{2}I_{RMS}\sin\left(\omega_e t + \frac{2\pi}{3}\right) \end{cases} \tag{6}$$

The AC winding MMF F_{ABC} is illustrated in Fig. 5, where F_A, F_B, and F_C are the A-, B-, and C-phase MMFs, respectively. The AC winding MMF F_{ABC} can be given by

$$\begin{cases} F_{ABC}\left(\delta,t\right) = S_{ABC}\sum_{n=1}^{\infty} M_{ABCn}\sin q \\ q = \begin{cases} -4n\delta + N_r\Omega_r t & n = 3r-2 \\ 4n\delta + N_r\Omega_r t & n = 3r-1 \\ 0 & n = 3r \end{cases} \end{cases} \tag{7}$$

where S_{ABC}=$3\sqrt{2}\,N_{ac}I_{RMS}/\pi$, M_{ABCn}=$\sin(4n\theta_3)/n$, ω_e is the electric frequency, and ω_e is $N_r\Omega_r$.

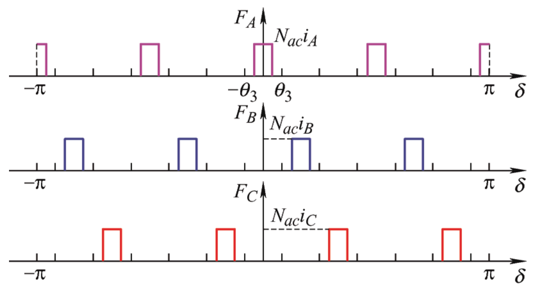

Fig. 5 Illustration of AC windings MMF F_{ABC}

3.3 Inner air-gap flux density and DC-winding-induced voltage harmonics

The inner air-gap flux density $B_i(\delta, t)$ can be given by

$$B_i\left(\delta,t\right) = F\left(\delta,t\right)\Lambda_i\left(\delta,t\right) \tag{8}$$

where $F(\delta, t)$ is the air-gap MMF. When the saturation in the lamination steel is neglected, it can be expressed as

$$F\left(\delta,t\right) = F_f\left(\delta\right) + F_{ABC}\left(\delta,t\right) \tag{9}$$

Combining Eqs. (1), (3), (5) and (7)-(9), the inner air-gap flux density $B_i(\delta, t)$ harmonic orders consist of p, q, and $|\alpha\pm\beta|$ (α=a, b, c or d, β=p or q). Since only rotating field harmonics can induce voltage pulsation, and the parameters a and p are time-invariant, as shown in Eqs. (4) and (5), there is no DC-coil-induced voltage due to p or $|a\pm p|$. Hence, the rotating inner air-gap field harmonics can be calculated and are listed in Tab. 3.

Tab. 3 Rotating inner air-gap field harmonics

No.	MMF	Spatial harmonic orders	Spatial harmonic orders in 12/10-pole machine	Rotating electric speed, ω_e	Amplitude $\propto$
1	F_f	$b\pm p$	$10j\pm6\times(2m-1)$	j	$S_{ir}I_f$
2		$c\pm p$	$10j\pm6\times[2(m\pm i)-1)]$	j	$S_{ir}S_{is}I_f$
3		$d\pm p$	$10j\pm6\times(2(m\mp i)-1]$	j	$S_{ir}S_{is}I_f$
4	F_{ABC}	q	$10-6\times[2(r-1)-1)]$	1	I_{RMS}
			$10-6\times(2r-1)$	1	
			$10+6\times[2(r-1)-1)]$	1	
			$10-6\times[2(r+1)-1)]$	–1	
5		$a\pm q$	$10+6\times[2(r\pm i-1)-1)]$	1	$S_{is}I_{RMS}$
			$10-6\times[2(r\pm i+1)-1)]$	1	
6		$b\pm q$	$10\times(j\pm1)\pm6\times[2(r-1)-1)]$	$j\pm1$	$S_{ir}I_{RMS}$
			$10\times(j\pm1)\mp6\times[2(r+1)-1)]$	$j\pm1$	
7		$c\pm q$	$10\times(j\pm1)\pm6\times[2(r\pm i-1)-1)]$	$j\pm1$	$S_{ir}S_{is}I_{RMS}$
			$10\times(j\pm1)\pm6\times[2(-r\pm i)-1)]$	$j\pm1$	
8		$d\pm q$	$10\times(j\pm1)\pm6\times[2(r\mp i-1)-1)]$	$j\pm1$	
			$10\times(j\pm1)\pm6\times[2(-r\mp i)-1)]$	$j\pm1$	

As shown in Tab. 3, the open-circuit DC winding MMF harmonics No. 1-3 will induce the j^{th} order harmonics in DC coils, where j is the harmonic order of $\Lambda_{ir}(\delta, t)$ given in Eq. (2b). When the position of the rotor iron bridge is closer to the inner air gap, that is, when d_{ib} is larger, the inner air-gap rotor saliency, and hence Λ_2 in Fig. 3b and S_{ir} in Eq. (2b), is smaller. When the rotor iron bridge is adjacent to the inner air gap, that is, when d_{ib} achieves the maximum value d_{ibmax}=2.5 mm, S_{ir} is zero. Hence, the amplitudes of the No. 1-3 harmonics in Tab. 3 are zero. This means that the open-circuit DC-winding-induced voltage can be theoretically reduced to zero by designing an inner air-gap adjacent rotor iron bridge.

For the on-load operation condition, a zero inner air-gap rotor saliency, and hence a S_{ir}=0, is also helpful in reducing the inner air-gap field harmonic amplitudes due to the armature reaction AC windings MMF in Tab. 3. By reducing the amplitudes of the No. 6-8 harmonics to zero, only No. 4 and No. 5 harmonics remain for the on-load operation condition. This means that the on-load DC-winding-induced voltage can also be reduced by designing a rotor iron bridge adjacent to the inner air gap.

4 Finite element verification

As concluded by the analytical analysis in Section 3, it is recommended to design the rotor iron bridge in the PS-WFSF machine adjacent to the inner air gap closer to the DC winding to achieve a smoother inner air-gap magnetic reluctance and hence a low DC-winding-induced voltage. This can be verified by the FE predicted influence of the position of the rotor iron bridge on the DC-winding-induced voltage and average electromagnetic torque, as shown in Fig. 6. Both the peak-to-peak values of the open-circuit and on-load DC-winding-induced voltages E_{open} and E_{load} reduced with a higher d_{ib}. Owing to the reduced air-gap field harmonic amplitudes, the average electromagnetic torque T_a is also smaller with a larger d_{ib}. Compared with the machine with d_{ib}=0, the average torque T_a of the machine with d_{ib}=2.5 mm will be slightly reduced by 7.41% from 2.18 N • m to 2.03 N • m, as shown in Fig. 7. However, the average electromagnetic torque of the original PS-WFSF machine without an iron bridge is T_a=2.93 N • m, as shown in Tab. 2.

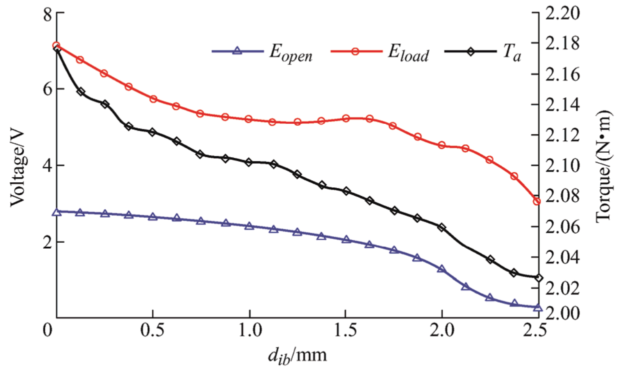

Fig. 6 FE predicted variation of DC-winding-induced voltage and average electromagnetic torque with the position of rotor iron bridge

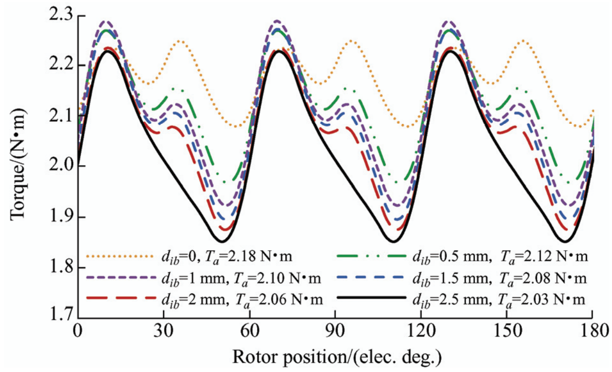

Fig. 7 On-load electromagnetic torque waveform for various d_{ib} (BLAC, i_d=0)

Fig. 8 shows the FE predicted inner air-gap radial flux densities in the machine with d_{ib}=0 and d_{ib}=2.5 mm. As shown in Fig. 8, most of the static harmonics in the machine with d_{ib}=2.5 mm are higher owing to the increment in average inner air-gap permeance. However, these static field harmonics cannot generate the induced voltage in DC winding. Both open-circuit and on-load inner air-gap rotating field harmonics can be effectively suppressed by designing an inner air-gap adjacent rotor iron bridge with d_{ib}=2.5 mm, verifying the analysis in Section 3.

As shown in Tab. 2, the open-circuit DC-winding-induced voltage predicted by the analytical model can be reduced to zero by designing d_{ib}=2.5 mm. However, as shown in Fig. 9, it has some non-zero harmonics due to the lamination steel saturation, which is neglected in the analytical model in Section 3. As a result, E_{open} can be reduced by 89.92% from 2.78 V in the machine with d_{ib}=0 to 0.28 V with d_{ib}=2.5 mm.

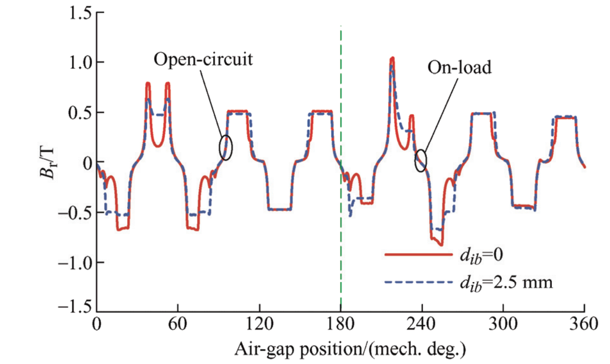

(a) Waveforms

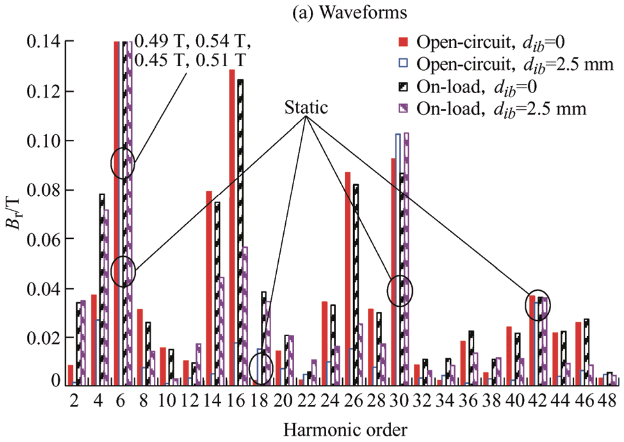

(b) Spectra

Fig. 8 Comparison of the FE predicted inner air-gap radial flux density

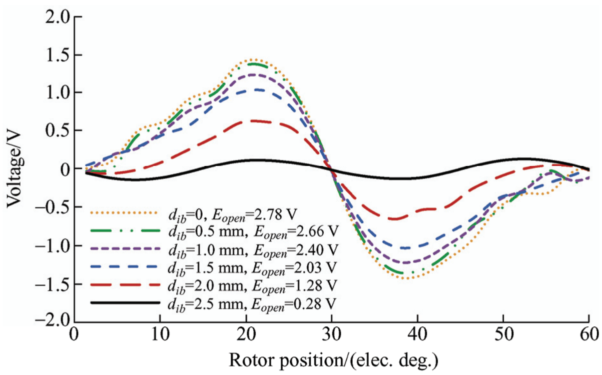

(a) Waveforms

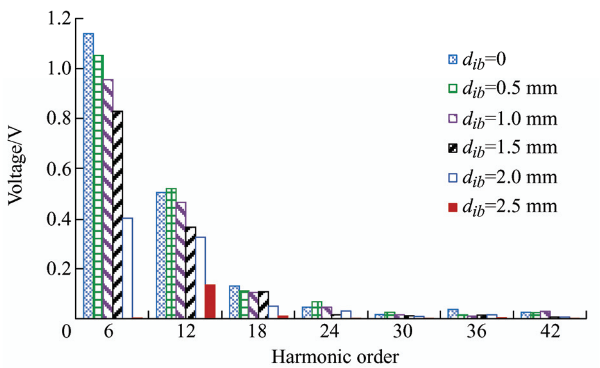

(b) Spectra

Fig. 9 Open-circuit DC-winding-induced voltages at 400 r/min for various d_{ib}

As shown in Fig. 10, E_{load} can be reduced by 57.28% from 7.14 V in the machine with d_{ib}=0 to 3.05 V in the machine with d_{ib}=2.5 mm. However, not all harmonics achieve the smallest value when d_{ib}=2.5 mm. As shown in Fig. 10b, a smaller 6^{th} harmonic can be obtained when d_{ib}=1 mm. This is caused by the lamination steel saturation and the various initial phases for different inner air-gap spatial harmonics with a $6\omega_e$ rotating electric speed—all of which generate the 6^{th} DC-winding-induced voltage harmonic.

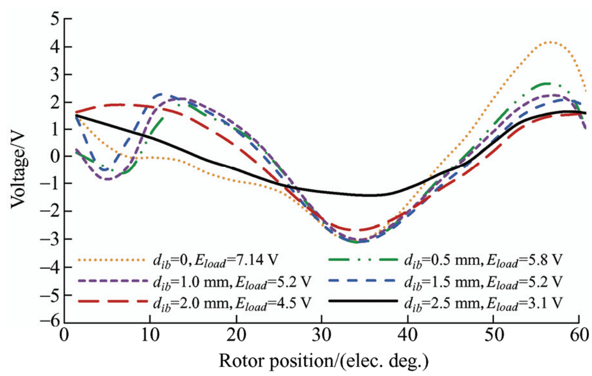

(a) Waveforms

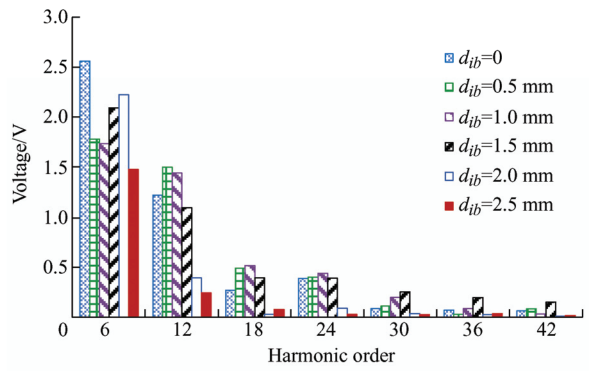

(b) Spectra

Fig. 10 On-load DC-winding-induced voltages at 400 r/min for various d_{ib}

5 Experimental validation

Since the machine with d_{ib}=2.5 mm exhibits the smallest DC-winding-induced voltage, it is built and tested to validate the previous analytical and FE analyses, as shown in Fig. 11.

(a) Outer stator

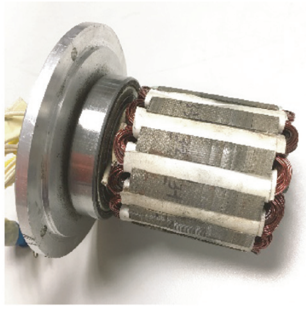

(b) Inner stator

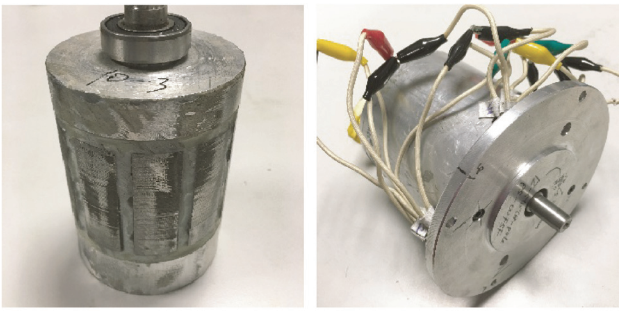

(c) Rotor (d) Assembled prototype

Fig. 11 Photos of the 12/10-pole PS-WFSF prototype with d_{ib}=2.5 mm

Since the influence of the DC power supply on the induced voltage cannot be separated, the induced voltage of the entire DC winding but that of DC coil 2 is measured [15]. DC coils 2k (k=1, 2, 3, ⋯, 6) are open-circuited, while the rest are connected in series with a doubled current for the same DC winding MMF.

Fig. 12 and Fig. 13 show the measured open-circuit and on-load DC coil 2 induced voltages of the prototype at 400 r/min, respectively. As shown in Fig. 14, both agree well with their counterparts predicted by FE, as well as the phase-A winding back-EMF. This trend also applies to the static torque, as shown in Fig. 15.

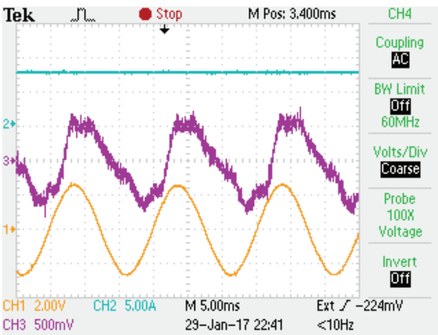

Fig. 12 Measured open-circuit A-phase winding back-EMF (CH1), DC winding current (CH2), and DC coil 2 induced voltage (CH3)

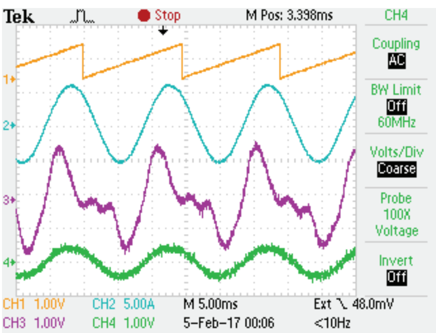

Fig. 13 Measured on-load rotor electric position (CH1), A-phase winding current (CH2), DC coil 2 induced voltage (CH3), and A-phase winding voltage (CH4)

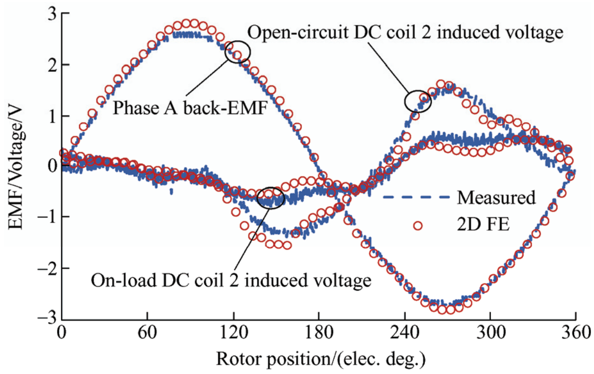

Fig. 14 Variation of measured and FE predicted A-phase winding back-EMF, open-circuit and on-load DC coil 2 induced voltages at 400 r/min

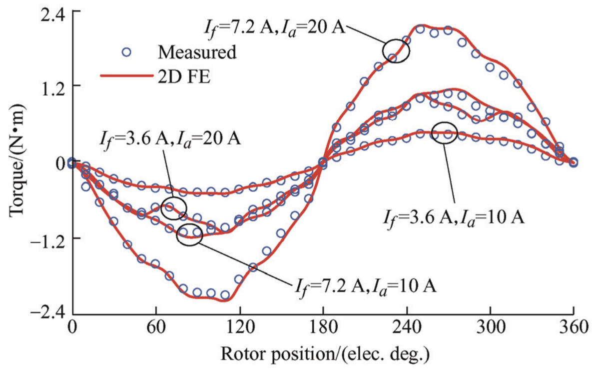

Fig. 15 Variation of measured and FE predicted static torques (I_a=−2I_b=−2I_c)

6 Conclusions

In this study, the influence of the position of the rotor iron bridge on the DC-winding-induced voltage in a PS-WFSF machine is investigated. Based on the MMF-permeance model, the air-gap harmonics of the PS-WFSF machine were analyzed. This shows that a proper iron bridge position can help reduce air-gap harmonics, and hence the DC-winding-induced voltage. As predicted by the analytical model and verified by the FE model, it is recommended to design the rotor iron bridge adjacent to the inner air gap closer to the DC winding. This is to achieve a smoother inner air-gap magnetic reluctance and hence a lower DC-winding-induced voltage, although the average electromagnetic torque is slightly reduced.

References

[1] Z Q Zhu, D Howe. Electrical machines and drives for electric, hybrid and fuel cell vehicles. *Proc. IEEE*, 2007, 95(4): 746-765.

[2] M Cheng, W Hua, J Z Zhang, et al. Overview of stator-permanent magnet brushless machines. *IEEE Trans. Ind. Electron.*, 2011, 58(11): 5087-5101.

[3] K T Chau, C C Chan, C H Liu. Overview of permanent-magnet brushless drives for electric and hybrid electric vehicles. *IEEE Trans. Indus. Electron.*, 2008, 55(6): 2246-2257.

[4] J Q Zheng, W X Zhao, J H Ji, et al. Sleeve design of permanent-magnet machine for low rotor losses. *Chinese Journal of Electrical Engineering*, 2020, 6(4): 86-96.

[5] I Boldea, L N Tutelea, L Parsa, et al. Automotive electric propulsion systems with reduced or no permanent magnets: An overview. *IEEE Trans. Ind. Electron.*, 2014, 61(10): 5696-5711.

[6] H J Liu, L Y Xu, M Z Shangguan, et al. Finite element analysis of 1 MW high speed wound-rotor synchronous machine. *IEEE Trans. Magn.*, 2012, 48(11): 4650-4653.

[7] M Y Ma, Z Z Wang, Q Q Yang, et al. Vector control strategy of a T-type three-level converter driving a switched reluctance motor. *Chinese Journal of Electrical Engineering*, 2019, 5(4): 15-21.

[8] C Pollock, M Wallace. The flux switching motor, a DC motor without magnets or brushes. *in Conf. Rec. IEEE IAS Annu. Meeting*, 1999, 3: 1980-1987.

[9] Y Tang, J J H Paulides, T E Motoasca, et al. Flux-switching machine with DC excitation. *IEEE Trans. Magn.*, 2012, 48(11): 3583-3586.

[10] L Xu, G H Liu, W X Zhao, et al. Design and analysis of a new linear wound-field flux reversal machine based on magnetic gear effect. *IEEE Trans. Magn.*, 2015, 51(11): 8205004.

[11] Z R Zhang, Y G Yan, Y Y Tao. A new topology of low speed doubly salient brushless DC generator for wind power generation. *IEEE Trans. Magn.*, 2012, 48(3): 1227-1233.

[12] S F Jia, R J Qu, J Li, et al. Principles of stator DC winding excited vernier reluctance machines. *IEEE Trans. Energy Convers.*, 2016, 31(3): 935-946.

[13] A Zulu, B Mecrow, A Armstrong. A wound-field three-phase flux switching synchronous motor with all excitation sources on the stator. *IEEE Trans. Ind. Appl.*, 2010, 46(6): 2363-2371.

[14] Z Q Zhu, Z Z Wu, D J Evans, et al. A wound field switched flux machine with field and armature windings separately wound in double stators. *IEEE Trans. Energy Convers.*, 2015, 30(2): 772-783.

[15] Z Z Wu, Z Q Zhu, C Wang, et al. Reduction of open-circuit DC winding induced voltage in wound field switched flux machines by skewing. *IEEE Trans. Ind. Electron.*, 2019, 66(3): 1715-1726.

[16] Z Z Wu, Z Q Zhu, C Wang, et al. Influence of position of rotor iron bridge on DC winding induced voltage in partitioned stator wound field switched flux machine. *in Proc. of CEFC*, 2018: 1-1.

[17] A Toba, T A Lipo. Novel dual-excitation permanent magnet Vernier machine. *in Proc. IEEE IAS Annu. Conf.,* Phoenix, US, 1999, 4: 2539-2544.

[18] Z Y Zong, L Quan, Y M Ge. A new double-stator flux-switching permanent magnet machine for electric vehicle application. *in Rec. of Intermag.*, Dresden, Germany, 2014: GP-5.

[19] Y B Wang, M Cheng, Y Du, et al. Design of high-torque-density double-stator permanent magnet brushless motors. *IET Electr. Power Appl.*, 2011, 5(3): 317-323.

[20] Y X Zhang, M Y Zhang, W M Ma, et al. Modeling of a double-stator linear induction motor. *IEEE Trans. Energy Convers.*, 2012, 27(3): 572-579.

[21] M Abbasian, M Moallem, B Fahimi. Double-stator switched reluctance machines (DSSRM): Fundamentals and magnetic force analysis. *IEEE Trans. Energy Convers.*, 2010, 25(3): 589-597.

[22] A H Isfahani, B Fahimi. Comparison of mechanical vibration between a double-stator switched reluctance machine and a conventional switched reluctance machine. *IEEE Trans. Magn.*, 2014, 50(2): 293-296.

[23] J C Yu, C H Liu, S Y Liu, et al. Comparative study of double-stator interior-PM vernier machines based on electromagnetic-structural coupling analysis. *IEEE Trans. Ind. Electron.*, DOI: 10.1109/TIE.2020.3034848.

[24] N W Frank, H A Toliyat. Analysis of the concentric planetary magnetic gear with strengthened stator and interior permanent magnet inner rotor. *IEEE Trans. Ind. Appl.*, 2011, 47(4): 1652-1660.

[25] M Cheng, P Han, W Hua. General airgap field modulation theory for electrical machines. *IEEE Trans. Ind. Electron.*, 2017, 64(8): 6063-6074.

[26] Z Z Wu, Z Q Zhu. Analysis of air-gap field modulation and magnetic gearing effects in switched flux permanent magnet machines. *IEEE Trans. on Magn.*, 2015, 51(5): 1-12.

[27] B Heller, V Hamata. Harmonic field effects in induction machines. Amsterdam: Elsevier, 1977.

[28] D W Li, R H Qu, J Li, et al. Synthesis of flux switching permanent magnet machines. *IEEE Trans. Energy Convers.*, 2016, 31(1): 106-117.

Zhongze Wu (S'15-M'18) received the B.Eng. and M.Sc. degrees in Electrical Engineering from Southeast University, Nanjing, China, in 2010 and 2013, respectively, and the Ph.D. degree in Electrical and Electronic Engineering from The University of Sheffield, Sheffield, UK, in January 2017.

Since March 2021, he has been with School of Electrical Engineering, Southeast University, Nanjing, China, as a Researcher. His major research interests include the advanced electrical machines and drives for electric propulsion systems.

From January 2017 to August 2018, he was with Warwick Manufacturing Group (WMG), University of Warwick, Coventry, UK, as a Research Fellow in electrical machines. From August 2018 to August 2020, he was with the Institute for Advanced Automotive Propulsion Systems (IAAPS), Department of Mechanical Engineering, University of Bath, Bath, UK, as a Prize Fellow, where he was a Lecturer between August 2020 and January 2021.

Z. Q. Zhu (M'90-SM'00-F'09) received the B.Eng. and M.Sc. degrees in Electrical and Electronic Engineering from Zhejiang University, Hangzhou, China, in 1982 and 1984, respectively, and the Ph.D. degree in Electrical and Electronic Engineering from The University of Sheffield, Sheffield, UK, in 1991.

Since 1988, he has been with The University of Sheffield, where he is currently a Research Chair of the Royal Academy of Engineering/Siemens with the Department of Electronic and Electrical Engineering and the Head of the Electrical Machines and Drives Research Group. His current research interests include the design and control of permanent-magnet brushless machines and drives for applications ranging from automotive through domestic appliances to renewable energy.

Dr. Zhu is a Fellow of the Royal Academy of Engineering.

Chao Wang received the B.Eng. and M.Sc. degrees in Electrical Engineering from Hefei University of Technology, Hefei, China, in 2008 and 2011, respectively, and the Ph.D. degree in Electronic and Electrical Engineering from The University of Sheffield, Sheffield, UK, in 2019.

Since 2019, he has been with Midea Welling Motor Technology Company, Ltd., Shanghai, China, as an Advanced Research Engineer, where he was an Engineer from 2011 to 2015. His research interests include the control of electric drives.

Wei Hua (M'03-SM'16) received the B.Sc. and Ph.D. degrees in Electrical Engineering from Southeast University, Nanjing, China, in 2001 and 2007, respectively. From 2004 to 2005, he was with the Department of Electronics and Electrical Engineering, The University of Sheffield, UK, as a Joint-Supervised Ph.D. Student.

Since 2007, he has been with Southeast University, where he is currently a Chief Professor of Southeast University and a Distinguished Professor of Jiangsu Province. From 2010, he has also worked with Yancheng Institute of New Energy Vehicles of Southeast University. He has co-authored over 150 technical papers. He holds 50 patents in his areas of interest. His teaching and research interests include design, analysis, and control of electrical machines, especially for PM brushless machines and switching reluctance machines, etc.

Kai Wang (M'13-SM'14) received the B.Eng. degree from China Jiliang University, Hangzhou, China, in 2004 and the Ph.D. degree from Zhejiang University, Hangzhou, China, in 2009.

From 2009 to 2010, he was with the Memorial University of Newfoundland, St. John's, NL, Canada, as a Postdoctoral Fellow. From 2010 to 2013, he was with The University of Sheffield, Sheffield, U.K. From 2013 to 2015, he was a Research Associate with the Sheffield Siemens Wind Power Research Centre, Sheffield, U.K., and a Research and Development Engineer with Ansys Inc., Canonsburg, PA, USA. Since 2015, he has been with the College of Automation Engineering, Nanjing University of Aeronautics and Astronautics, Nanjing, China. His current research interests include the design and control of permanent-magnet machines.

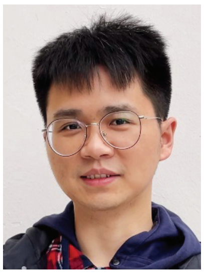

Wentao Zhang was born in Suzhou, China, in 1995. He received the B.Eng. degree in Electrical Engineering and Its Automation in July 2018 from Southeast University, Nanjing, China, where he has been working toward the M.Sc. degree since September 2018.

His major research interests include the design, analysis, and control of the wound field switched flux machines.